


 Cite this: *RSC Adv.*, 2021, 11, 34533

# Insight into the Fischer–Tropsch mechanism on hcp-Fe<sub>7</sub>C<sub>3</sub> (211) by density functional theory: the roles of surface carbon and vacancies†

 Jie Ren,<sup>ab</sup> Ning Ai <sup>\*a</sup> and Yingzhe Yu <sup>\*b</sup>

Iron carbide phases discovered in the spent iron catalysts have proved to be active in the Fischer–Tropsch process. The surface carbon of the iron carbide played a key role in the Fischer–Tropsch mechanism. Since there are two surface carbons, C1 and C2, on the hcp-Fe<sub>7</sub>C<sub>3</sub> (211), which are close to each other, their reaction mechanisms would be significant. Hence, the DFT calculations were performed to investigate the Fischer–Tropsch mechanism involving the surface carbon. It was found that the HC<sup>1</sup> + C<sup>2</sup> pathway was the major C–C coupling reaction pathway with an effective energy barrier of 0.97 eV. Ethane would be the major C<sub>2</sub> product from the HC<sup>1</sup>C<sup>2</sup> species through the stepwise hydrogenation pathway due to the high adsorption energy of ethylene (1.67 eV). After the desorption process of ethane, the carbon vacancy would form. The carbon vacancy was found to be the CO activation site through the CO direct dissociation pathway and the carbon vacancy would recover. It was concluded that the defect-hcp-Fe<sub>7</sub>C<sub>3</sub> (211) is the high active facet of the Fischer–Tropsch synthesis, the carbon vacancy sites are the CO activation sites and the surface carbon sites are the C–C coupling sites. The surface carbons not only act as the chain initiation sites but also act as the chain growth sites in the Fischer–Tropsch mechanism on hcp-Fe<sub>7</sub>C<sub>3</sub> (211).

 Received 24th August 2021  
 Accepted 8th October 2021

 DOI: 10.1039/d1ra06396k  
[rsc.li/rsc-advances](http://rsc.li/rsc-advances)

## Introduction

Fischer–Tropsch synthesis (FTS) is a promising process since it can convert syngas into liquid fuels and chemicals so that other carbon-based energy such as coal and biomass can be utilized.<sup>1,2</sup> The FTS process has been studied for a long time for the production of long-chain fuels.<sup>3,4</sup> In a recent study, the Fischer–Tropsch synthesis was proved to produce light olefins with acceptable selectivity.<sup>5,6</sup> Iron-based catalysts are usually selected as fundamental catalysts for the production of light olefins.<sup>7–10</sup> The promoter addition is one of the major modifications,<sup>11–14</sup> while the design of specific catalyst structures is another optimization method for improving the catalyst performance.<sup>15,16</sup> However, the selectivity of light olefins in the hydrocarbon species over the iron catalysts cannot meet the economic demand in the industry.<sup>17</sup> As a result, the performance of the iron catalysts requires urgent improvement.

Nowadays, there are different kinds of iron-containing phases in the spent iron catalysts.<sup>18–23</sup> The major iron carbide

phases are ε-Fe<sub>2</sub>C, ε-Fe<sub>2.2</sub>C, Fe<sub>7</sub>C<sub>3</sub>, γ-Fe<sub>5</sub>C<sub>2</sub>, θ-Fe<sub>3</sub>C, and so on.<sup>24,25</sup> γ-Fe<sub>5</sub>C<sub>2</sub> and ε-Fe<sub>2</sub>C have been proved to be the active phases in the iron catalysts.<sup>26,27</sup> θ-Fe<sub>3</sub>C is always considered as the inactive phase as it mainly appears in deactivated iron-based catalysts.<sup>28,29</sup> Fe<sub>7</sub>C<sub>3</sub> would be present after a long run and high-temperature Fischer–Tropsch synthesis,<sup>30,31</sup> which has been proved to be the active phase by Brent Williams *et al.* and Yongwang Li *et al.*<sup>32,33</sup>

A comprehensive understanding of the Fischer–Tropsch mechanism on the iron catalysts would assist the researcher to improve the catalysis performance. Since the iron catalysts are composed of different iron carbide phases, the Fischer–Tropsch mechanism on the iron catalysts is also composed of the Fischer–Tropsch mechanism on different iron carbide phases. Thus, it is necessary to investigate the Fischer–Tropsch mechanism on each iron carbide phase, especially the one that was proved to be active in the Fischer–Tropsch synthesis. However, the preparation, characterization, and exploration of the single iron carbide phase under the reaction conditions are difficult. As a result, the theoretical method is used for investigating the Fischer–Tropsch mechanism on the single iron carbide phase and is applied in this research.

To date, the Fischer–Tropsch mechanism is clear for some iron carbide phases. Thanh Hai Pham *et al.* pointed out that the direct CO dissociation reaction and the coupling reaction of C + HC or HC + HC are the major CO activation pathway and chain-growth pathway, respectively, on the γ-Fe<sub>5</sub>C<sub>2</sub> (510).<sup>34,35</sup> After

<sup>a</sup>College of Biological, Chemical Sciences and Engineering, Jiaxing University, Jiaxing 314001, P. R. China. E-mail: aining@tsinghua.org.cn

<sup>b</sup>Key Laboratory for Green Chemical Technology of Ministry of Education, R&D Center for Petrochemical Technology, Tianjin University, Tianjin 300072, P. R. China. E-mail: yuyingzhe@tju.edu.cn

† Electronic supplementary information (ESI) available. See DOI: 10.1039/d1ra06396k



that, the influence of the H coverage effect on the Fischer-Tropsch mechanism was introduced by Minhua Zhang *et al.* Due to the existence of the H coverage effect, the CO insertion mechanism rather than the carbide mechanism is the Fischer-Tropsch mechanism on the  $\chi$ -Fe<sub>5</sub>C<sub>2</sub> (510).<sup>36</sup> The CO activation mechanism on the  $\chi$ -Fe<sub>5</sub>C<sub>2</sub> (001),  $\chi$ -Fe<sub>5</sub>C<sub>2</sub> (221),  $\chi$ -Fe<sub>5</sub>C<sub>2</sub> (010),  $\chi$ -Fe<sub>5</sub>C<sub>2</sub> (110),  $\chi$ -Fe<sub>5</sub>C<sub>2</sub> (111) has been discussed thoroughly by Yurong He *et al.*<sup>37,38</sup> On  $\theta$ -Fe<sub>3</sub>C (100)<sup>39</sup> and  $\theta$ -Fe<sub>3</sub>C (010),<sup>40</sup> the CO insertion dissociation pathway is the major CO activation mechanism and the C-C coupling mechanism. On  $\theta$ -Fe<sub>3</sub>C (031), the coupling reaction of HC + HC and H<sub>2</sub>C + H<sub>2</sub>C is the major chain-growth pathway.<sup>41</sup> However, the Fischer-Tropsch mechanism on other iron carbide phases has not yet been discussed thoroughly.

As mentioned before, the hcp-Fe<sub>7</sub>C<sub>3</sub> phase has been proved to be active in Fischer-Tropsch synthesis by experimental research.<sup>32,33</sup> In previous research, DFT calculations were applied to investigate the CO activation pathway on hcp-Fe<sub>7</sub>C<sub>3</sub> (211).<sup>42</sup> The results showed that CO would undergo the H-assisted dissociation pathway on the top site rather than the CO insertion dissociation pathway with the surface carbon. However, the C-C coupling pathway and the product formation pathway on hcp-Fe<sub>7</sub>C<sub>3</sub> (211) are not clear. Thus, this article aims to investigate the Fischer-Tropsch mechanism on the hcp-Fe<sub>7</sub>C<sub>3</sub> phase so that the understanding of the iron catalyst's mechanism could be improved.

According to the known mechanism on other iron carbide phases, the surface carbon that belongs to the catalyst would participate in the Fischer-Tropsch synthesis. On the Fe<sub>2</sub>C (011), Fe<sub>5</sub>C<sub>2</sub> (010), Fe<sub>3</sub>C (001), and Fe<sub>4</sub>C (100), the surface carbon was found to be the carbon source of the product methane.<sup>43</sup> On the  $\chi$ -Fe<sub>5</sub>C<sub>2</sub> (510), the surface carbon would undergo a stepwise hydrogenation reaction to give the H<sub>x</sub>C species. Then the H<sub>x</sub>C species can participate in the subsequent C-C coupling reaction.<sup>34-36</sup> On  $\theta$ -Fe<sub>3</sub>C (100) and  $\theta$ -Fe<sub>3</sub>C (010),<sup>39,40</sup> the surface carbon would act as the chain initiation site so that the reactant CO could be coupled with it to accomplish the CO activation pathway and chain-growth pathway. Other than theoretical work, Khodakov *et al.* proved that the initiation of chain growth involves the surface carbon through isotope C13 research.<sup>44</sup> As a result, the surface carbon would always play a key role in the Fischer-Tropsch mechanism.

The previously researched model of hcp-Fe<sub>7</sub>C<sub>3</sub> (211) showed that two surface carbons are close to each other, leading to the problem of what role they play in the Fischer-Tropsch mechanism. Hence, when the DFT calculations were performed to accomplish the full map of the Fischer-Tropsch mechanism on hcp-Fe<sub>7</sub>C<sub>3</sub> (211), the surface carbon was considered to be the significant reactant and was thoroughly discussed in the designed reaction pathway.

In short, as the iron catalysts are combined with different kinds of iron carbide phases, including the hcp-Fe<sub>7</sub>C<sub>3</sub> phase, the research on the Fischer-Tropsch mechanism on the hcp-Fe<sub>7</sub>C<sub>3</sub> phase would be valuable in the iron catalysts and deserves to be researched. The experimental research on the reaction mechanism in the pure hcp-Fe<sub>7</sub>C<sub>3</sub> phase would be difficult since the specific iron carbide would be transferred to another kind of

iron carbide under the Fischer-Tropsch synthesis. Hence, DFT calculations are applied in this article to investigate the Fischer-Tropsch mechanism on the hcp-Fe<sub>7</sub>C<sub>3</sub> (211) facet, because it possesses the largest percentage among the exposed crystal facets.

We expect that this research will provide a better comprehension of the Fischer-Tropsch mechanism on the hcp-Fe<sub>7</sub>C<sub>3</sub> phase so that the iron-based catalysts can be understood clearly and be modified efficiently.

## Computational details

### Surface model

In this study, the bulk hcp-Fe<sub>7</sub>C<sub>3</sub> was selected as the bulk catalyst according to the experimental results.<sup>33</sup> The hcp-Fe<sub>7</sub>C<sub>3</sub> belongs to the hexagonal system with the *P6<sub>3</sub>mc* space group. The lattice constants of hcp-Fe<sub>7</sub>C<sub>3</sub> are  $a = 6.826 \text{ \AA}$ ;  $b = 6.826 \text{ \AA}$ ;  $c = 4.495 \text{ \AA}$ ;  $\gamma = 120^\circ$ . The bulk structure of hcp-Fe<sub>7</sub>C<sub>3</sub> was optimized with a  $3 \times 3 \times 5$  Monkhorst-Pack *k*-point mesh. The optimized lattice constants are  $a = 6.748 \text{ \AA}$ ;  $b = 6.748 \text{ \AA}$ ;  $c = 4.434 \text{ \AA}$ ;  $\gamma = 120^\circ$ , which are in agreement with the experimental values. The hcp-Fe<sub>7</sub>C<sub>3</sub> (211) facet possesses the largest percentage among the exposed crystal facets based on the surface energy calculation<sup>36</sup> and the XRD results (PDF #89-7273).<sup>45</sup> The surface reactions were calculated on a  $p(1 \times 1)$  hcp-Fe<sub>7</sub>C<sub>3</sub> (211) slab with a stable terminal surface. The size of the  $p(1 \times 1)$  hcp-Fe<sub>7</sub>C<sub>3</sub> (211) slab is  $a = 11.14 \text{ \AA}$ ;  $b = 8.074 \text{ \AA}$ , which could avoid the interactions between the adsorbate with itself in the neighbouring repeated images. In all calculations, the bottom two Fe layers were fixed in their bulk position, while the top two Fe layers and the adsorbents were allowed to relax. The top view and side view of the hcp-Fe<sub>7</sub>C<sub>3</sub> (211) slab model are shown in Fig. 1.

### First-principles calculations

The spin-polarized DFT calculations were performed *via* the projector augmented wave (PAW) method<sup>46-48</sup> using the Vienna

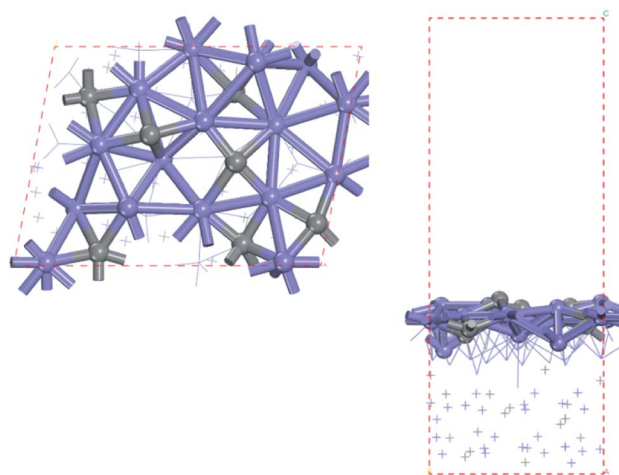


Fig. 1 Top (left) and side (right) views of hcp-Fe<sub>7</sub>C<sub>3</sub> (211) surface (blue: Fe atoms; gray: C atoms).



*ab initio* simulation package (VASP). In this article, the Perdew–Burke–Ernzerhof (PBE) functional<sup>49</sup> with the plane wave cutoff energy of 400 eV was applied. The Brillouin zone sampling of the bulk calculation and the surface calculation were set as  $3 \times 3 \times 5$  and  $2 \times 2 \times 1$  Monkhorst–Pack grids,<sup>50</sup> respectively. The electron smearing was employed *via* the Methfessel–Paxton technique with a smearing width consistent with 0.2 eV.<sup>51</sup> The effects of van der Waals corrections were taken into account by the DFT-D3 method with Becke–Johnson (BJ) damping.<sup>52,53</sup>

The convergence standard of the SCF calculation and the geometry optimization were set as  $1 \times 10^{-5}$  eV and  $0.03 \text{ eV \AA}^{-1}$ , respectively. The climbing-image nudged elastic band method (CI-NEB)<sup>54,55</sup> was selected to search the transition state and to evaluate the intrinsic energy barrier. The convergence standard of the CI-NEB calculation was set as  $0.05 \text{ eV \AA}^{-1}$ . The frequency calculation was performed to confirm the TS structure after the CI-NEB calculation. Only if the TS structure of the researched elementary reaction has only one imaginary frequency can the TS structure be confirmed.

The adsorption energy of surface species is defined and calculated by  $E_{\text{ads}} = E(\text{adsorbate/slab}) - [E(\text{slab}) + E(\text{adsorbate})]$ , in which  $E(\text{adsorbate/slab})$  is the energy of the slab with surface adsorbate,  $E(\text{slab})$  is the energy of the slab, and  $E(\text{adsorbate})$  is the energy of the free adsorbate. The reaction energy and the intrinsic energy barrier are calculated by  $\Delta E_r = E(\text{FS}) - E(\text{IS})$  and  $E_a = E(\text{TS}) - E(\text{IS})$ , respectively, where  $E(\text{IS})$ ,  $E(\text{FS})$ , and  $E(\text{TS})$  are the energies of the corresponding initial state (IS), final state (FS), and transition state (TS), respectively.

The reaction pathways researched in the article are combined with a series of consecutive reactions. For an elementary reaction, if the coverage of the reactant is extremely low, the reaction rate would be slow due to the mass law, even though the intrinsic energy barrier of this elementary reaction is not high. As a result, the determination of the major reaction pathway based only on the intrinsic energy barrier would be doubtful. In order to solve such a problem, the effective energy barrier<sup>56–58</sup> was applied to evaluate the major reaction pathway. The effective energy barrier of the  $k^{\text{th}}$  elementary reaction in the consecutive reactions is represented by  $E_{\text{eff},k}$  and is calculated

by  $E_{\text{eff},k} = E_{a,k} + \sum_i^{k-1} \Delta E_{r,i}$ . In the equation,  $E_{a,k}$  is the intrinsic

energy barrier of the  $k^{\text{th}}$  step elementary reaction,  $\sum_i^{k-1} \Delta E_{r,i}$  is the sum of the reaction energy from the  $i^{\text{th}}$  step elementary reaction to the  $(k-1)^{\text{th}}$  step elementary reaction and the  $i^{\text{th}}$  step elementary reaction is the elementary reaction whose initial state shows the lowest electronic energy among all the states of the studied consecutive reactions.

In the consecutive reactions, there are some elementary reactions, which are the transfer reaction of the surface species from one adsorption site to another, or the structure transformation reaction; these two types of reactions are named migration reactions in this article. Most of the migration reactions show relatively low intrinsic energy barrier in this article, the computational intrinsic energy barrier of each migration reaction can be found in the ESI.† To avoid the energy profile

diagram being tedious and unreadable, only the reaction energies of migration reactions are taken into account in the energy profile diagram, which is named as migration energy and denoted as  $\Delta E_m$ .

In short, when the migration energy is applied in the energy profile diagram, the effective energy barrier of the  $k^{\text{th}}$  elementary reaction in the consecutive reactions is calculated by

$$E_{\text{eff},k} = E_{a,k} + \sum_i^{k-1} \Delta E_{r,i} + \sum_i^{k-1} E_{m,i}, \text{ where the } \sum_i^{k-1} \Delta E_{m,i} \text{ is the sum}$$

of the migration energy from the  $i^{\text{th}}$  elementary reaction in the consecutive reactions to the  $(k-1)^{\text{th}}$  elementary reaction in the consecutive reactions.

## Results and discussion

### The C–C coupling reactions of the surface carbon

Fig. 2 shows the sites of the major carbon-containing species (in the red box) on hcp-Fe<sub>7</sub>C<sub>3</sub> (211), which are the C1 site, C2 site, and HC site, based on the previous research.<sup>43</sup> The C<sup>1</sup> site and C<sup>2</sup> site are the surface carbons that belong to the catalysts. The C<sup>1</sup> species and C<sup>2</sup> species are the hydrogenation products of the surface carbon. The HC site is the CO activation site of the H-assisted CO activation pathway and the HC species is the product of the known CO activation pathway.

Since the H-assisted CO activation pathway is the known CO activation mechanism, the carbide mechanism seems to be the major Fischer–Tropsch mechanism on the Fe<sub>7</sub>C<sub>3</sub> (211). The detailed possible designed reaction pathway is shown below: (1) the CO adsorption process (2) the CO activation process on the HC site. (3) The C–C coupling process of H<sub>x</sub>C species with the C<sup>1</sup> species or C<sup>2</sup> species to be the C<sub>2</sub> species (4) The hydrogenation process, the product desorption process, or chain-growth process of the C<sub>2</sub> species. (5) The recovery process of C<sup>1</sup> or C<sup>2</sup>.

All the surface carbon-containing species are the possible reactants of the C–C coupling reaction. Before starting to calculate and research the C–C coupling process of H<sub>x</sub>C species with C<sup>1</sup> species or C<sup>2</sup> species, it should be noted that the distance from the C<sup>1</sup> site to the C<sup>2</sup> site is close to the distance from the HC site to the C<sup>1</sup> site, and the distance from the HC site to the C<sup>2</sup> site as shown in Fig. 2.

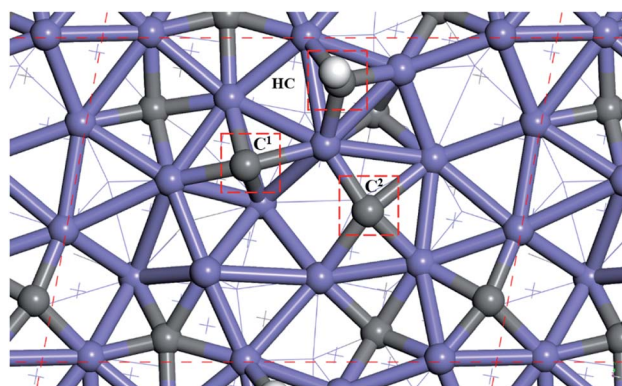
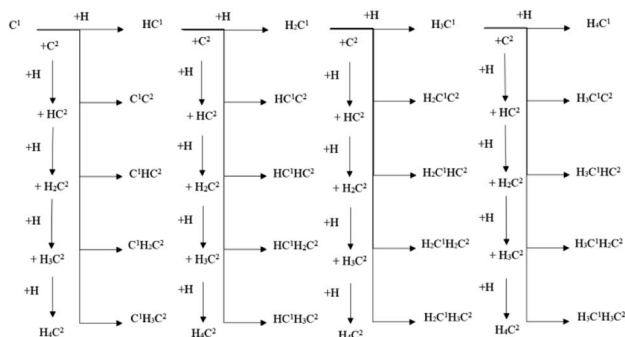


Fig. 2 The site of major carbon-containing species on hcp-Fe<sub>7</sub>C<sub>3</sub> (211).



**Table 1** The distance of the C atom between the C<sup>1</sup> site, C<sup>2</sup> site and HC site on hcp-Fe<sub>7</sub>C<sub>3</sub> (211)

Distance between C atom(Å)	C <sup>1</sup>	C <sup>2</sup>	HC
C <sup>1</sup>	—	3.212	3.205
C <sup>2</sup>	—	—	3.460
CH	—	—	—



**Scheme 1** The designed C<sup>1</sup>-C<sup>2</sup> coupling pathways on hcp-Fe<sub>7</sub>C<sub>3</sub> (211).

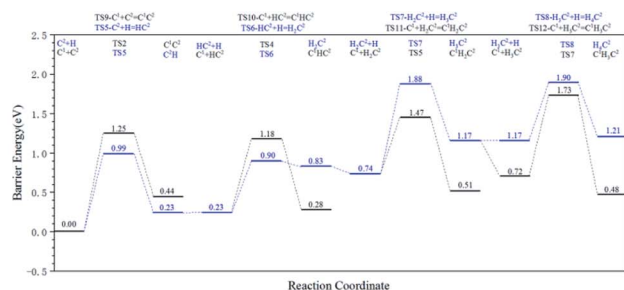
The distances between the C<sup>1</sup> site, C<sup>2</sup> site, and HC site were calculated and shown in Table 1. The results show that the distance from the C<sup>1</sup> site to the C<sup>2</sup> site, the distance from the HC site to the C<sup>1</sup> site, and the distance from the HC site to C<sup>2</sup> site are 3.212 Å, 3.205 Å, and 3.460 Å, respectively, and are close.

**Table 2** The intrinsic energy barriers ( $E_a$ , eV), reaction energies ( $E_r$ , eV) and migration energies ( $E_m$ , eV) of the C<sup>1</sup>-C<sup>2</sup> coupling pathway

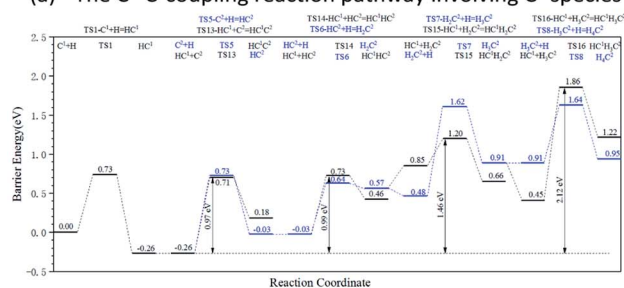
No	Reaction	$E_m$	$E_a$	$E_r$
1	C <sup>1</sup> + H = HC <sup>1</sup>	0	0.73	-0.26
2	HC <sup>1</sup> + H = H <sub>2</sub> C <sup>1</sup>	0	0.73	0.71
3	H <sub>2</sub> C <sup>1</sup> + H = H <sub>3</sub> C <sup>1</sup>	0.09	0.91	0.48
4	H <sub>3</sub> C <sup>1</sup> + H = H <sub>4</sub> C <sup>1</sup>	0	0.60	0.03
5	C <sup>2</sup> + H = HC <sup>2</sup>	0	0.99	0.23
6	HC <sup>2</sup> + H = H <sub>2</sub> C <sup>2</sup>	0	0.67	0.60
7	H <sub>2</sub> C <sup>2</sup> + H = H <sub>3</sub> C <sup>2</sup>	-0.09	1.14	0.43
8	H <sub>3</sub> C <sup>2</sup> + H = H <sub>4</sub> C <sup>2</sup>	0	0.83	0.04
9	C <sup>1</sup> + C <sup>2</sup> = C <sup>1</sup> C <sup>2</sup>	0	1.25	0.44
10	C <sup>1</sup> + HC <sup>2</sup> = C <sup>1</sup> HC <sup>2</sup>	0	0.95	0.05
11	C <sup>1</sup> + H <sub>2</sub> C <sup>2</sup> = C <sup>1</sup> H <sub>2</sub> C <sup>2</sup>	-0.09	1.05	0.26
12	C <sup>1</sup> + H <sub>3</sub> C <sup>2</sup> = C <sup>1</sup> H <sub>3</sub> C <sup>2</sup>	-0.45	0.97	0.10
13	HC <sup>1</sup> + C <sup>2</sup> = HC <sup>1</sup> C <sup>2</sup>	0	0.97	0.44
14	HC <sup>1</sup> + HC <sup>2</sup> = HC <sup>1</sup> HC <sup>2</sup>	0	0.76	0.46
15	HC <sup>1</sup> + H <sub>2</sub> C <sup>2</sup> = HC <sup>1</sup> H <sub>2</sub> C <sup>2</sup>	0.39	0.87	0.28
16	HC <sup>1</sup> + H <sub>3</sub> C <sup>2</sup> = HC <sup>1</sup> H <sub>3</sub> C <sup>2</sup>	-0.46	1.43	0.38
17	H <sub>2</sub> C <sup>1</sup> + C <sup>2</sup> = H <sub>2</sub> C <sup>1</sup> C <sup>2</sup>	0	0.73	-0.23
18	H <sub>2</sub> C <sup>1</sup> + HC <sup>2</sup> = H <sub>2</sub> C <sup>1</sup> HC <sup>2</sup>	0	0.74	0.20
19	H <sub>2</sub> C <sup>1</sup> + H <sub>2</sub> C <sup>2</sup> = H <sub>2</sub> C <sup>1</sup> H <sub>2</sub> C <sup>2</sup>	-0.09	0.83	-0.27
20	H <sub>2</sub> C <sup>1</sup> + H <sub>3</sub> C <sup>2</sup> = H <sub>2</sub> C <sup>1</sup> H <sub>3</sub> C <sup>2</sup>	-0.46	1.00	0.31
21	H <sub>3</sub> C <sup>1</sup> + C <sup>2</sup> = H <sub>3</sub> C <sup>1</sup> C <sup>2</sup>	-0.13	1.01	-0.24
22	H <sub>3</sub> C <sup>1</sup> + HC <sup>2</sup> = H <sub>3</sub> C <sup>1</sup> HC <sup>2</sup>	-0.17	1.41	0.77
23	H <sub>3</sub> C <sup>1</sup> + H <sub>2</sub> C <sup>2</sup> = H <sub>3</sub> C <sup>1</sup> H <sub>2</sub> C <sup>2</sup>	-0.34	1.45	0.31
24	H <sub>3</sub> C <sup>1</sup> + H <sub>3</sub> C <sup>2</sup> = H <sub>3</sub> C <sup>1</sup> H <sub>3</sub> C <sup>2</sup>	-0.62	2.92	0.10

As a result, if the H<sub>x</sub>C species can be coupled with the C<sup>1</sup> species or C<sup>2</sup> species, the C<sup>1</sup> species and C<sup>2</sup> species could also possibly couple with each other.

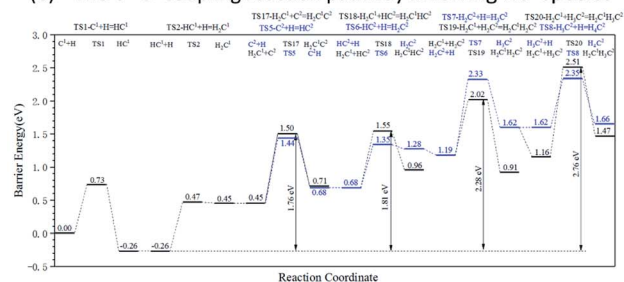
Hence, another possible C-C coupling pathway was presented, which is denoted as the C<sup>1</sup>-C<sup>2</sup> coupling pathway. In the C<sup>1</sup>-C<sup>2</sup> coupling pathway, the C<sup>1</sup> species and C<sup>2</sup> species can be coupled with each other to be C<sub>2</sub> species. Based on the new idea of the C<sup>1</sup>-C<sup>2</sup> coupling pathway, the designed reaction pathway is shown in Scheme 1 and the calculated results are shown in Table 2. It was



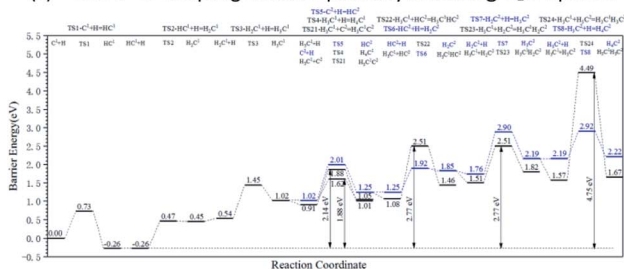
(a) The C<sup>1</sup>-C<sup>2</sup> coupling reaction pathway involving C<sup>1</sup> species



(b) The C<sup>1</sup>-C<sup>2</sup> coupling reaction pathway involving HC<sup>1</sup> species



(c) The C<sup>1</sup>-C<sup>2</sup> coupling reaction pathway involving H<sub>2</sub>C<sup>1</sup> species



(d) The C<sup>1</sup>-C<sup>2</sup> coupling reaction pathway involving H<sub>3</sub>C<sup>1</sup> species

**Fig. 3** Energy profile diagrams for the C<sup>1</sup>-C<sup>2</sup> coupling pathways on the hcp-Fe<sub>7</sub>C<sub>3</sub> (211) surface: (a) the C<sup>1</sup>-C<sup>2</sup> coupling reaction pathway involving C<sup>1</sup> species; (b) the C<sup>1</sup>-C<sup>2</sup> coupling reaction pathway involving HC<sup>1</sup> species; (c) the C<sup>1</sup>-C<sup>2</sup> coupling reaction pathway involving H<sub>2</sub>C<sup>1</sup> species; (d) the C<sup>1</sup>-C<sup>2</sup> coupling reaction pathway involving H<sub>3</sub>C<sup>1</sup> species. Black lines: the C-C coupling reaction pathways of different kinds of C<sup>1</sup> hydrocarbon species. Blue lines: the stepwise hydrogenation pathways of C<sup>2</sup> hydrocarbon species.



found that some of the coupling reactions showed relatively low energy barriers, which proved that the  $C^1$ - $C^2$  coupling pathway is likely to be the major C-C coupling pathway on the hcp-Fe<sub>7</sub>C<sub>3</sub> (211).

The energy profile diagrams of the  $C^1$ - $C^2$  coupling pathway are shown in Fig. 3. The  $C^1$ - $C^2$  coupling reaction pathway involving  $C^1$ ,  $HC^1$ ,  $H_2C^1$ , and  $H_3C^1$  species are present in Fig. 3(a-d) and were denoted as the  $C^1$  coupling pathway,  $HC^1$  coupling pathway,  $H_2C^1$  coupling pathway, and  $H_3C^1$  coupling pathway, respectively. The black line represents the C-C coupling reaction pathway involving the  $C^1$  species and  $C^2$  species. The blue line represents the stepwise hydrogenation pathway of the  $C^2$  hydrocarbon species.

Comparing the effective energy barriers of the coupling pathways involving different  $C^1$  species and  $C^2$  species, the major  $C^1$ - $C^2$  coupling pathway would be achieved. The  $HC^1 + C^2$  pathway showed the lowest effective energy barrier of 0.97 eV, while the effective energy barrier of the  $HC^1 + HC^2$  pathway is close to that of the  $HC^1 + C^2$  pathway (0.99 eV). The effective energy barriers of the  $C^1 + C^2$  pathway and the  $C^1 + HC^2$  pathway are a bit higher than that of the  $HC^1 + C^2$  pathway, which are 1.25 eV and 1.18 eV, respectively. The effective energy barriers of the  $C^1$ - $C^2$  coupling reactions involving  $H_2C$  species and  $H_3C$  species are much higher, making them impossible.

There are two major reasons why the C-C coupling reaction involving  $H_2C$  species and  $H_3C$  species would show high effective energy barriers. Firstly, Table 2 shows that in the  $C^1$  coupling pathway,  $HC^1$  coupling pathway, and  $H_2C^1$  coupling pathway, the intrinsic energy barrier of the C-C coupling reaction is not extremely high. However, the hydrogenation reactions of HC species are endothermic with high reaction energies, which are 0.71 eV and 0.60 eV for  $HC^1$  and  $HC^2$ , respectively. The high reaction energy of the HC hydrogenation reaction represents the instability of the  $H_2C$  species so that the dehydrogenation reaction of the  $H_2C$  species would take place easily. Hence, the degree of coverage of the  $H_2C$  species would be small on the hcp-Fe<sub>7</sub>C<sub>3</sub> (211). The small coverage of the reactant species would result in the slow reaction rate of the specific C-C coupling reaction involving  $H_2C$  species according to the mass law. Hence, the high effective energy barrier of the  $C^1$ - $C^2$  coupling pathways involving  $H_2C$  could be attributed to the high instability of the  $H_2C$  species. This situation was also found in other iron carbides from theoretical and experimental research.<sup>35,36</sup>

Secondly, Table 2 shows that the C-C coupling reactions involving  $H_3C$  species have high intrinsic energy barriers, which could be attributed to the weak interactions between the surface and  $H_3C$  species. To confirm the inference, Table 3 presents the Bader charge analysis on the  $C_1$  species. The “C”, “H<sup>1</sup>”, “H<sup>2</sup>”, and “H<sup>3</sup>” represent the number of “Bader charges” in specific atoms in the  $C_1$  species. The “charge transfer” represents the Bader charge transfer between the  $C_1$  species and hcp-Fe<sub>7</sub>C<sub>3</sub> (211), in which “+” represents the charge obtained by the  $C_1$  species from the hcp-Fe<sub>7</sub>C<sub>3</sub> (211).

Table 3 shows that the charge obtained by the  $C_1$  species from the hcp-Fe<sub>7</sub>C<sub>3</sub> (211) would decrease with the increase in H atoms in the  $C_1$  species. The decrease in the charge transfer indicates the decrease in the interactions between the  $C_1$  species and hcp-Fe<sub>7</sub>C<sub>3</sub> (211). The charge transfers of the  $H_3C^1$  species with the hcp-Fe<sub>7</sub>C<sub>3</sub> (211) and the  $H_3C^2$  species with the hcp-Fe<sub>7</sub>C<sub>3</sub> (211) were +0.30 and +0.35, respectively, which are much lower as compared to the other  $C_1$  species with the hcp-Fe<sub>7</sub>C<sub>3</sub> (211). Hence, the hcp-Fe<sub>7</sub>C<sub>3</sub> (211) could hardly activate the C-C coupling reaction involving the  $H_3C$  species so that the intrinsic energy barrier would be high as shown in Table 2. This phenomenon has also been found and reported on other iron carbides.<sup>36</sup>

The major  $C^1$ - $C^2$  coupling pathways were achieved and are shown in Scheme 2, including the  $C^1 + C^2$  pathway,  $HC^1 + C^2$  pathway,  $C^1 + HC^2$  pathway, and  $HC^1 + HC^2$  pathway. Among the major  $C^1$ - $C^2$  coupling pathways, the  $HC^1 + C^2$  pathway is the preferred  $C^1$ - $C^2$  coupling pathway with an effective energy barrier of 0.97 eV.

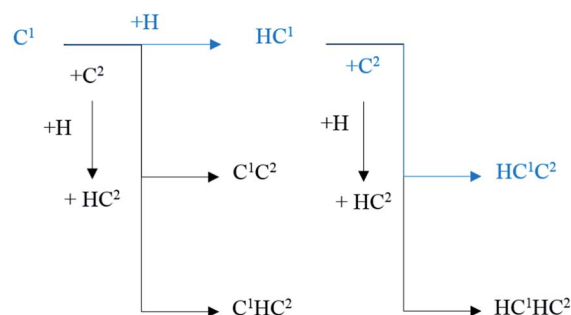
According to the results, a new possible C-C coupling pathway with a relatively low energy barrier was discovered and it could be the major C-C coupling mechanism. However, the preferred  $C^1$ - $C^2$  coupling pathway needs to be compared with other possible C-C coupling pathways to decide whether or not it could be the major C-C coupling mechanism.

The major possible C-C coupling mechanisms in the Fischer-Tropsch synthesis are the carbide mechanism and CO insertion mechanism.

On hcp-Fe<sub>7</sub>C<sub>3</sub> (211), the C-C coupling pathway through the CO insertion mechanism has been discussed thoroughly.<sup>43</sup> The effective energy barrier of the preferred C-C coupling pathway through the CO insertion mechanism is 1.48 eV, which is much

Table 3 The results of the Bader charge analysis on the  $C_1$  species on hcp-Fe<sub>7</sub>C<sub>3</sub> (211)

Species	C	H <sup>1</sup>	H <sup>2</sup>	H <sup>3</sup>	Total	Charge transfer
$C^1$	4.91	—	—	—	4.91	+0.91
$HC^1$	4.86	0.87	—	—	5.73	+0.73
$H_2C^1$	4.79	0.87	0.97	—	6.63	+0.63
$H_3C^1$	4.59	0.83	0.98	0.90	7.30	+0.30
$C^2$	4.92	—	—	—	4.92	+0.92
$HC^2$	4.88	0.88	—	—	5.76	+0.76
$H_2C^2$	4.78	0.90	0.97	—	6.65	+0.65
$H_3C^2$	4.48	0.94	0.98	0.95	7.35	+0.35



Scheme 2 The major  $C^1$ - $C^2$  coupling pathways (black lines) and preferred  $C^1$ - $C^2$  coupling pathways (blue lines) on hcp-Fe<sub>7</sub>C<sub>3</sub> (211).



higher than that of the preferred C<sup>1</sup>-C<sup>2</sup> coupling pathway. Thus, the C<sup>1</sup> species and the C<sup>2</sup> species prefer to be coupled with each other rather than with adsorbed CO.

Another possible C-C coupling pathway is the coupling reaction between surface carbon and H<sub>x</sub>C species through the carbide mechanism, in which the H<sub>x</sub>C species are the products through the H-assisted CO activation pathway. The effective energy barrier of the H<sub>x</sub>C species formation pathway is 1.30 eV, which is also higher than that of the preferred C<sup>1</sup>-C<sup>2</sup> coupling pathway. As a result, the effective energy barrier of the preferred C<sup>1</sup>-C<sup>2</sup> coupling pathway is much lower than those of the other two possible C-C coupling pathways. It can be concluded that on the hcp-Fe<sub>7</sub>C<sub>3</sub> (211), the C<sup>1</sup>-C<sup>2</sup> coupling pathway is the major C-C coupling mechanism of the C<sub>2</sub> species and the major coupling products are HC<sup>1</sup>C<sup>2</sup> and HC<sup>1</sup>HC<sup>2</sup> species.

### The stepwise hydrogenation pathway of the C<sub>2</sub> species

After the C-C coupling reaction pathway, the subsequent reaction pathways of the major C<sub>2</sub> species are the parts of the Fischer-Tropsch mechanism on the hcp-Fe<sub>7</sub>C<sub>3</sub> (211). The possible ensuing reaction pathways are the stepwise hydrogenation pathway and the subsequent C-C coupling pathway.

The discussion of the subsequent C-C coupling pathway would be almost the same as the C-C coupling pathway discussed before, except that the chain initiation site is the C<sub>2</sub> species rather than the C<sub>1</sub> species. Although the influence of the carbon chain length on the C-C coupling mechanism is important, it will not be discussed here.

The stepwise hydrogenation pathway of the C<sub>2</sub> species is another possible subsequent reaction pathway. The discussion of the stepwise hydrogenation pathway is necessary, as it could determine whether the major C<sub>2</sub> product on the hcp-Fe<sub>7</sub>C<sub>3</sub> (211) is acetylene, ethylene, or ethane.

The designed stepwise hydrogenation pathway is shown in Scheme 3. The idea of the designed stepwise hydrogenation pathway is the hydrogenation elementary reaction on C<sup>1</sup> and C<sup>2</sup> of each possible C<sub>2</sub> species from the initial C<sub>2</sub> species, C<sub>1</sub>C<sub>2</sub>. In each hydrogenation elementary reaction, the 3-fold H sites are thought of as the reactants. The adsorption sites and adsorption energy of possible 3-fold sites H have been discussed in the previous study.<sup>43</sup> The calculation results of the stepwise hydrogenation pathways are shown in Table 4.

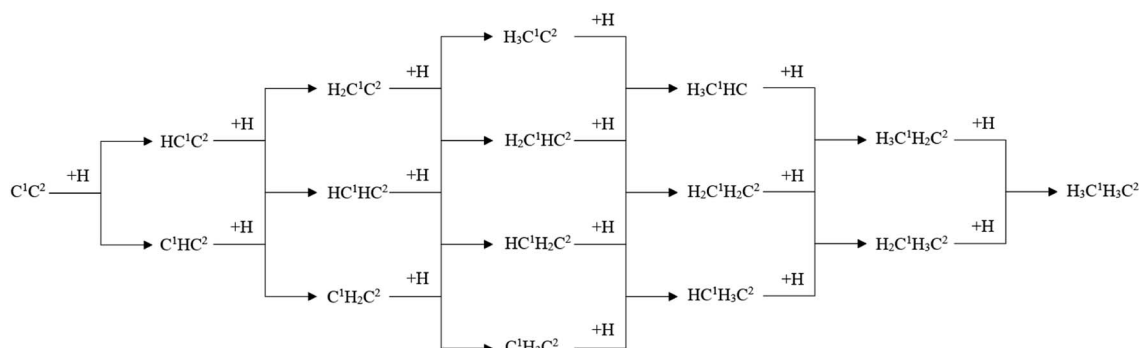
Table 4 The intrinsic energy barrier (*E<sub>a</sub>*, eV), reaction energy (*E<sub>r</sub>*, eV) and migration energy (*E<sub>m</sub>*, eV) of the C<sup>2</sup> stepwise hydrogenation pathway

No	Reaction	<i>E<sub>m</sub></i>	<i>E<sub>a</sub></i>	<i>E<sub>r</sub></i>
1	H + C <sup>1</sup> C <sup>2</sup> = HC <sup>1</sup> C <sup>2</sup>	0	0.78	-0.20
2	C <sup>1</sup> C <sup>2</sup> + H = C <sup>1</sup> HC <sup>2</sup>	0	0.96	-0.15
3	HC <sup>1</sup> C <sup>2</sup> + H = HC <sup>1</sup> HC <sup>2</sup>	0	0.65	0.27
4	C <sup>1</sup> HC <sup>2</sup> + H = C <sup>1</sup> H <sub>2</sub> C <sup>2</sup>	0.11	0.68	0.28
5	H + HC <sup>1</sup> C <sup>2</sup> = H <sub>2</sub> C <sup>1</sup> C <sup>2</sup>	0	0.79	0.38
6	H + C <sup>1</sup> HC <sup>2</sup> = HC <sup>1</sup> HC <sup>2</sup>	0.29	0.73	0.08
7	H + H <sub>2</sub> C <sup>1</sup> C <sup>2</sup> = H <sub>3</sub> C <sup>1</sup> C <sup>2</sup>	0	0.59	0.39
8	H <sub>2</sub> C <sup>1</sup> C <sup>2</sup> + H = H <sub>2</sub> C <sup>1</sup> HC <sup>2</sup>	-0.10	0.27	0.19
9	H + C <sup>1</sup> H <sub>2</sub> C <sup>2</sup> = HC <sup>1</sup> H <sub>2</sub> C <sup>2</sup>	0.42	0.62	0.15
10	HC <sup>1</sup> HC <sup>2</sup> + H = HC <sup>1</sup> H <sub>2</sub> C <sup>2</sup>	0	1.04	0.62
11	C <sup>1</sup> H <sub>2</sub> C <sup>2</sup> + H = C <sup>1</sup> H <sub>3</sub> C <sup>2</sup>	0	1.13	0.41
12	H + HC <sup>1</sup> HC <sup>2</sup> = H <sub>2</sub> C <sup>1</sup> HC <sup>2</sup>	0	1.21	0.81
13	H <sub>3</sub> C <sup>1</sup> C <sup>2</sup> + H = H <sub>3</sub> C <sup>1</sup> HC <sup>2</sup>	0.02	0.69	0.66
14	H + HC <sup>1</sup> H <sub>2</sub> C <sup>2</sup> = H <sub>2</sub> C <sup>1</sup> H <sub>2</sub> C <sup>2</sup>	0	0.66	0.33
15	HC <sup>1</sup> H <sub>2</sub> C <sup>2</sup> + H = HC <sup>1</sup> H <sub>3</sub> C <sup>2</sup>	0.10	0.67	0.20
16	H <sub>2</sub> C <sup>1</sup> HC <sup>2</sup> + H = H <sub>2</sub> C <sup>1</sup> H <sub>2</sub> C <sup>2</sup>	0	0.60	0.11
17	H + H <sub>2</sub> C <sup>1</sup> HC <sup>2</sup> = H <sub>3</sub> C <sup>1</sup> HC <sup>2</sup>	0	0.74	0.44
18	H + C <sup>1</sup> H <sub>3</sub> C <sup>2</sup> = HC <sup>1</sup> H <sub>3</sub> C <sup>2</sup>	0	1.22	1.17
19	H <sub>2</sub> C <sup>1</sup> H <sub>2</sub> C <sup>2</sup> + H = H <sub>2</sub> C <sup>1</sup> H <sub>3</sub> C <sup>2</sup>	0.10	0.47	0.25
20	H + H <sub>2</sub> C <sup>1</sup> H <sub>2</sub> C <sup>2</sup> = H <sub>3</sub> C <sup>1</sup> H <sub>2</sub> C <sup>2</sup>	0	0.95	0.89
21	H + HC <sup>1</sup> H <sub>3</sub> C <sup>2</sup> = H <sub>2</sub> C <sup>1</sup> H <sub>3</sub> C <sup>2</sup>	0	0.99	0.51
22	H <sub>3</sub> C <sup>1</sup> HC <sup>2</sup> + H = H <sub>3</sub> C <sup>1</sup> H <sub>2</sub> C <sup>2</sup>	0	0.76	0.46
23	H + H <sub>2</sub> C <sup>1</sup> H <sub>3</sub> C <sup>2</sup> = H <sub>3</sub> C <sup>1</sup> H <sub>3</sub> C <sup>2</sup>	0	0.87	0.16
24	H <sub>3</sub> C <sup>1</sup> H <sub>2</sub> C <sup>2</sup> + H = H <sub>3</sub> C <sup>1</sup> H <sub>3</sub> C <sup>2</sup>	0	0.99	-0.05

Table 4 shows that the intrinsic energy barrier and reaction energy of the hydrogenation reaction are not high, which indicates that both the hydrogenation reaction and the dehydrogenation reaction could take place.

The energy profile diagram of the stepwise hydrogenation pathway based on the hydrogenation elementary reactions in Table 4 is shown in Fig. 4. The diagram can be divided into two parts: the hydrogenation reactions on C<sup>1</sup> (black lines) and the hydrogenation reactions on C<sup>2</sup> (blue lines). The green lines represent products that could be formed from both kinds of hydrogenation reactions.

According to Fig. 4, the HC<sup>1</sup>C<sup>2</sup> species is the most stable species among the C<sub>2</sub> species on hcp-Fe<sub>7</sub>C<sub>3</sub> (211). Since most hydrogenation reactions of the HC<sup>1</sup>C<sup>2</sup> species and their hydrogenation products are endothermic, the effective energy



Scheme 3 The designed stepwise hydrogenation pathway of C<sub>2</sub> species on hcp-Fe<sub>7</sub>C<sub>3</sub> (211).



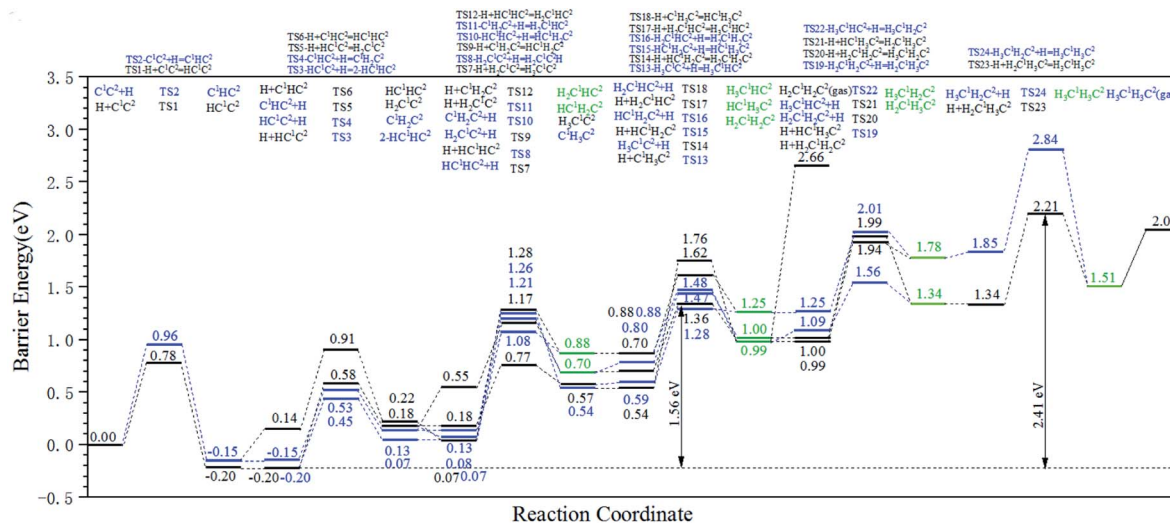
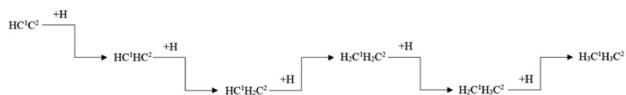


Fig. 4 Energy profile diagram for the stepwise hydrogenation pathway of  $C_2$  species on the hcp- $Fe_7C_3$  (211) surface. Black lines: hydrogenation reactions occurring on  $C^1$ . Blue lines: hydrogenation reactions occurring on  $C^2$ . Green lines: products from both kinds of hydrogenation reactions.

barrier of the hydrogenation reactions would increase gradually along with the increase of H atoms in the reactant.

Ethylene and ethane are two major  $C_2$  products in the Fischer–Tropsch synthesis. The effective energy barriers of the ethylene formation pathway and the ethane formation pathway are 1.56 eV and 2.41 eV, respectively. It seems that ethylene would be the major  $C_2$  product since the effective energy barrier of the ethylene formation pathway is much lower than that of the ethane formation pathway. However, the ethylene adsorption energy is 1.67 eV, which is much higher than the intrinsic energy barrier of the ethylene hydrogenation reaction (0.47 eV). As a result, the hydrogenation reaction of the ethylene adsorption would take place more easily than the ethane adsorption. The adsorption energy of ethane (0.53 eV) is lower than the intrinsic energy barrier of the ethane dehydrogenation reaction (0.70 eV). Hence, the adsorbed ethane could escape from the hcp- $Fe_7C_3$  (211) easily to form the ethane product. As a result, the ethane formation pathway is thought to be the major  $C_2$  stepwise hydrogenation pathway. The detailed ethane formation pathway is shown in Scheme 4. The effective energy barrier of the ethane formation pathway is 2.41 eV, which is much higher than that of the preferred C–C coupling pathway and the CO activation pathway. The stepwise hydrogenation pathway would be the rate-determining step.

The over-hydrogenation of the  $C_2$  species resulted in the ethane being the major  $C_2$  product on hcp- $Fe_7C_3$  (211) in the Fischer–Tropsch synthesis. This could mainly be attributed to the strong interactions between the hcp- $Fe_7C_3$  (211) and the adsorbed ethylene, which is characterized by the high adsorption energy of the adsorbed ethylene. Hence, if the target



Scheme 4 The preferred stepwise hydrogenation pathway of the  $C_2$  coupling product on hcp- $Fe_7C_3$  (211).

product in the Fischer–Tropsch synthesis is the olefin, the over-hydrogenation phenomenon should be suppressed.

#### The surface recovery pathway for the defect-hcp- $Fe_7C_3$ (211)

From the previous section,  $C^1$  and  $C^2$  are the surface carbons of the hcp- $Fe_7C_3$  (211) and they could be a part of the product through the  $C^1$ – $C^2$  coupling pathway, as well as the stepwise hydrogenation pathway. Regardless of the type of hydrocarbon, once the products are desorbed from the surface, the two carbon vacancy sites would form, which are denoted as the Cv1 site and Cv2 site, and the surface is denoted as the defect-hcp- $Fe_7C_3$  (211).

The structure of the defect-hcp- $Fe_7C_3$  (211) is different from that of the hcp- $Fe_7C_3$  (211). To allow the discovered Fischer–Tropsch reaction pathway to be repeatable and the discussed Fischer–Tropsch mechanism to make sense, the defect-hcp- $Fe_7C_3$  (211) should be able to recover to the hcp- $Fe_7C_3$  (211). Due to the CO being the major feedstock in the Fischer–Tropsch synthesis, the adsorption and activation pathways of CO on the Cv1 site and Cv2 site are thought to be the possible surface recovery pathway, which is denoted as the carbon vacancy recovery pathway.

The designed carbon vacancy recovery pathway contained three kinds of elementary reactions after the CO adsorption on the Cv1 site or the Cv2 site, which are the hydrogenation reactions on the carbon site, the hydrogenation reactions on the oxygen site, and the dissociation reactions of C–O bonds.

The computation results are shown in Table 5. The intrinsic energy barrier of the elementary reaction in the carbon vacancy recovery pathway is a bit high, which indicates that the carbon vacancy recovery pathway may occur with difficulty.

The energy profile diagram of the carbon vacancy recovery pathway is shown in Fig. 5. The blue line represents the carbon vacancy recovery pathway in the Cv1 site and the black line represents the carbon vacancy recovery pathway in the Cv2 site.



**Table 5** The intrinsic energy barrier ( $E_a$ , eV), the reaction energy ( $E_r$ , eV), and migration energy ( $E_m$ , eV) of the reactions in the carbon vacancy recovery pathway

No	Reaction	$E_m$	$E_a$	$E_r$
1	$H + C^1O = HC^1O$	0	1.04	1.03
2	$C^2O = C^2 + O$	0	1.18	-0.75
3	$H + C^2O = HC^2O$	0	1.27	1.13
4	$C^1O = C^1 + O$	0	1.37	0.17
5	$C^1O + H = C^1OH$	0	1.58	0.81
6	$C^2O + H = C^2OH$	0	1.66	1.04
7	$HC^1O = HC^1 + O$	0	0.46	-0.90
8	$H + HC^1O = H_2C^1O$	0	0.89	0.65
9	$HC^1O + H = HC^1OH$	0	1.64	1.15

On the Cv1 site, in the first step, the HCO formation reaction showed a relatively low intrinsic energy barrier of 1.04 eV. However, in the subsequent reactions, the effective energy barrier of the HCO dissociation reaction would be high (1.49 eV) because of the high instability of HCO species. At the same time, the intrinsic energy barriers of the CO dissociation reaction and COH formation reaction were 1.37 eV and 1.58 eV, respectively. As a result, the dissociation reaction of the adsorbed CO is the preferred carbon vacancy recovery pathway in the Cv1 site.

On the Cv2 site, among the three kinds of elementary reactions in the carbon vacancy recovery pathway, the CO dissociation reaction shows the lowest intrinsic energy barrier (1.18 eV). The intrinsic energy barriers of the HCO formation pathway and COH formation pathway are 1.27 eV and 1.66 eV, respectively. Thus, the dissociation reaction of adsorbed CO is also the preferred carbon vacancy recovery pathway in the Cv2 site and the subsequent reactions of HCO species and COH species need not be taken into account.

From another perspective, the carbon vacancy recovery pathway is the CO activation pathway on carbon vacancy. Thus, the effective energy barriers of the CO activation pathway on the

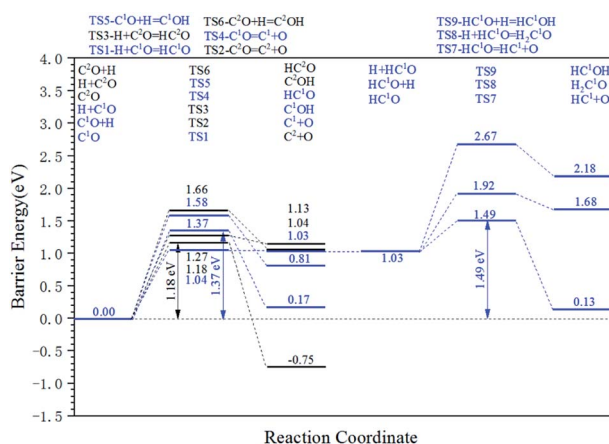
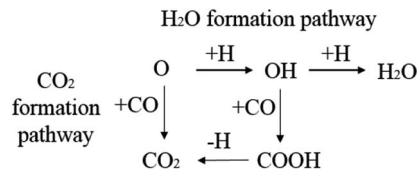


**Fig. 5** Energy profile diagram for the carbon vacancy recovery pathway on defect-hcp-Fe<sub>7</sub>C<sub>3</sub> (211). Blue lines: the carbon vacancy recovery pathway in the Cv1 site. Black lines: the carbon vacancy recovery pathway in the Cv2 site.



**Scheme 5** The designed oxygen removal pathways on hcp-Fe<sub>7</sub>C<sub>3</sub> (211).

Cv1 site and the Cv2 site are 1.37 eV and 1.18 eV, respectively, which are close to the effective energy barrier of the H-assisted CO activation pathway on the top site (1.30 eV).

The results above indicate that the carbon vacancy is the possible CO activation site. Since the C<sup>1</sup>-C<sup>2</sup> coupling pathway is the major C-C coupling mechanism, the surface carbon would be consumed rapidly so that the carbon vacancy would form frequently. Hence, it could be inferred that the C vacancy, especially the Cv2 site, is the major CO activation site.

After completing the carbon vacancy recovery pathway, the dissociation oxygen would be left on the hcp-Fe<sub>7</sub>C<sub>3</sub> (211). The accumulation of surface oxygen would result in the changing of the iron carbide phase. As a result, whether the surface oxygen could be removed from the surface efficiently is the last piece of the puzzle to confirm the Fischer-Tropsch mechanism achieved in this article.

CO<sub>2</sub> or H<sub>2</sub>O are the major products of the surface oxygen on the iron catalysts. Therefore, the H<sub>2</sub>O formation pathway and CO<sub>2</sub> formation pathway are set as the designed oxygen removal pathways, shown in Scheme 5. The computation results are shown in Table 6.

The energy profile diagram of the oxygen removal pathway is shown in Fig. 6. In the first step, the intrinsic energy barriers of the O + H pathway and O + CO pathway are 1.30 eV and 1.40 eV, respectively, which are close. In the subsequent reaction, the desorption energy of CO<sub>2</sub> is 0.53 eV, which is much lower than the intrinsic energy barrier of the OH + H pathway and OH + CO pathway. As a result, the CO<sub>2</sub> formation pathway is the preferred oxygen removal pathway with a relatively low effective energy barrier (1.50 eV), while the H<sub>2</sub>O formation pathway is suppressed due to the high effective energy barrier of 2.01 eV.

In brief, the surface recovery pathway contains the C recovery vacancy pathway and the oxygen removal pathway is clear. The effective energy barrier of the preferred C recovery vacancy pathway in the Cv1 site, the preferred C recover vacancy pathway in the Cv2 site, and the oxygen removal pathway are 1.37 eV,

**Table 6** The intrinsic energy barrier ( $E_a$ , eV), the reaction energy ( $E_r$ , eV), and migration energy ( $E_m$ , eV) of the reactions in the oxygen removal pathway

No	Reaction	$E_m$	$E_a$	$E_r$
1	$O + H = OH$	0	1.30	0.53
2	$O + CO = CO_2$	0	1.40	0.87
3	$OH + CO = COOH$	-0.01	1.24	0.89
4	$OH + H = H_2O$	-0.01	1.49	0.87
5	$COOH = CO_2 + H$	-0.02	0.70	-0.30



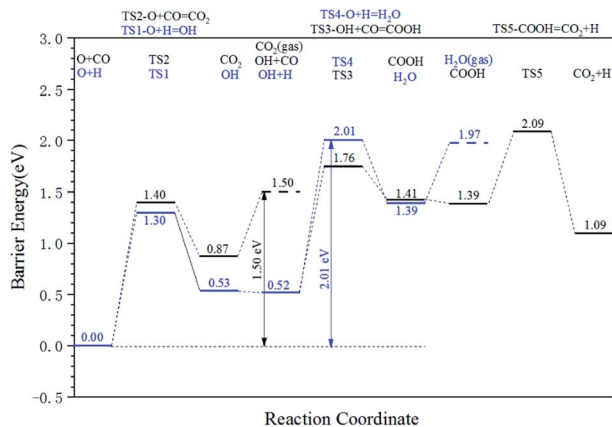


Fig. 6 Energy profile diagram for oxygen removal pathways on hcp-Fe<sub>7</sub>C<sub>3</sub> (211). Blue lines: the H<sub>2</sub>O formation pathways. Black lines: the CO<sub>2</sub> formation pathways.

1.18 eV, and 1.50 eV, respectively. The effective energy barrier of the preferred surface recovery pathway is higher than that of the major C–C coupling mechanism but lower than the preferred C<sub>2</sub> stepwise hydrogenation pathway. Hence, it could be proved that if the C<sub>2</sub> product could be properly produced through the preferred C<sub>2</sub> stepwise hydrogenation pathway, the defect-hcp-Fe<sub>7</sub>C<sub>3</sub> (211) could also possibly recover to the hcp-Fe<sub>7</sub>C<sub>3</sub> (211). The presence of the surface recovery pathway could confirm that the studied surface is stable under the Fischer–Tropsch synthesis reaction conditions and the Fischer–Tropsch mechanism achieved above is universal on hcp-Fe<sub>7</sub>C<sub>3</sub> (211).

### The full map of the Fischer–Tropsch mechanism and the role of the surface carbon on hcp-Fe<sub>7</sub>C<sub>3</sub> (211)

According to the discussion in this article, the full map of the Fischer–Tropsch mechanism on hcp-Fe<sub>7</sub>C<sub>3</sub> (211) can be achieved. The achieved Fischer–Tropsch mechanism would begin with the adsorption of CO and the dissociation H, which are from the reactant syngas, and end with the C<sub>2</sub> product. The full map of the Fischer–Tropsch mechanism is shown in Scheme 6.

On hcp-Fe<sub>7</sub>C<sub>3</sub> (211), the Fischer–Tropsch mechanism can be divided into several parts. First, the C<sup>1</sup> would undergo the hydrogenation reaction to form the HC species. Second, the HC<sup>1</sup> species would be able to couple with the C<sup>2</sup> so that the HC<sup>1</sup>C<sup>2</sup> species would come into being. Third, the HC<sup>1</sup>C<sup>2</sup> species would form the ethane product through a stepwise hydrogenation pathway. Fourth, two carbon vacancy sites would form after the desorption of the ethane product, resulting in the changing of the hcp-Fe<sub>7</sub>C<sub>3</sub> (211) to the defect-hcp-Fe<sub>7</sub>C<sub>3</sub> (211).

Fifth, the CO would adsorb and dissociate directly on the C vacancy so that the C<sup>1</sup> and C<sup>2</sup> would recover. Sixth, the surface oxygen from the CO would be removed in the form of CO<sub>2</sub> and the Fischer–Tropsch synthesis would restart in the first step.

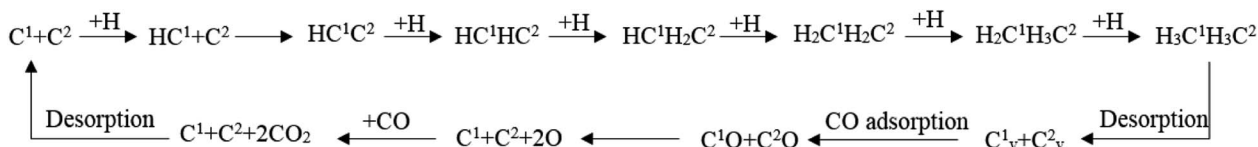
In the achieved Fischer–Tropsch mechanism, the effective energy barriers of the six steps are 0.73 eV, 0.97 eV, 2.41 eV, 0.53 eV, 1.37 eV and 1.50 eV, respectively. As a result, on the hcp-Fe<sub>7</sub>C<sub>3</sub> (211), the stepwise hydrogenation pathway is thought to be the rate-determining step of the Fischer–Tropsch mechanism. Hence, it could be inferred that the C<sub>2</sub> species and the C vacancy would accumulate on the hcp-Fe<sub>7</sub>C<sub>3</sub> (211) surface. Since the effective energy barrier of the C vacancy recovery pathway is not high, the Cv1 site and Cv2 site could act as the CO activation site to produce the C<sub>1</sub> species with the co-adsorption C<sub>2</sub> species. After that, the C–C coupling reaction could take place, possibly involving the C<sub>2</sub> species and C<sub>1</sub> species so that the length of the carbon chain would increase.

The adsorption energy of ethylene is high (1.67 eV). It could also be inferred that after the chain growth process, if the adsorption site of the long-chain olefins is on the same site, the adsorption energy of long-chain olefin would be close to that of ethylene, which would result in the alkane rather than the olefin being the major product on the hcp-Fe<sub>7</sub>C<sub>3</sub> (211).

During the Fischer–Tropsch mechanism, it was found that carbon vacancy sites are the CO activation pathway sites and the surface carbon sites are the C–C coupling pathway sites; the surface carbon and its vacancy play a key role in the Fischer–Tropsch mechanism on the hcp-Fe<sub>7</sub>C<sub>3</sub> (211).

As mentioned before, the surface carbon is always thought to be able to participate in the Fischer–Tropsch synthesis in iron carbide. On the other iron carbide, such as  $\chi$ -Fe<sub>5</sub>C<sub>2</sub> (510),  $\theta$ -Fe<sub>3</sub>C (100), and  $\theta$ -Fe<sub>3</sub>C (010), the surface carbon just acts as the chain initiation site, the C<sub>1</sub> species participating in the chain growth process are the CO-activated products from the surface sites.<sup>39,40</sup> On the hcp-Fe<sub>7</sub>C<sub>3</sub> (211), the surface carbon not only acts as the chain initiation site but also acts as the chain growth site. Hence, it could be concluded that on the hcp-Fe<sub>7</sub>C<sub>3</sub> (211), the total Fischer–Tropsch synthesis takes place on the vacancy site while on the other iron carbide, only a part of the Fischer–Tropsch synthesis takes place on the vacancy site. This property may result in the high reactant conversion and reaction rate of the Fischer–Tropsch synthesis.<sup>33</sup>

From another perspective, it is the defect-hcp-Fe<sub>7</sub>C<sub>3</sub> (211) rather than the hcp-Fe<sub>7</sub>C<sub>3</sub> (211) that is the high active facet of the Fischer–Tropsch synthesis. However, at first, the defect-hcp-Fe<sub>7</sub>C<sub>3</sub> (211) is not thought of as the stable surface to be researched. Based on this article, it could be found that under the Fischer–Tropsch synthesis conditions, the exposed surface



Scheme 6 The full map of the Fischer–Tropsch mechanism on hcp-Fe<sub>7</sub>C<sub>3</sub> (211).



would change and update with the influence of CO and H<sub>2</sub>. As a result, when researching the Fischer–Tropsch mechanism on the iron carbide phase through the theoretical method, the change in the selected surface structure should be taken into account, especially the change in the surface carbon.

According to the mechanism achieved in this article, the hcp-Fe<sub>7</sub>C<sub>3</sub> (211) shows high conversion of syngas, which is the advantage of the Fischer–Tropsch synthesis. However, the major products in the hcp-Fe<sub>7</sub>C<sub>3</sub> (211) would be the long-chain products or the alkane products, which is the disadvantage of the Fischer–Tropsch synthesis, especially when the target products are the light olefins. As a result, promoting or suppressing the formation of the hcp-Fe<sub>7</sub>C<sub>3</sub> phase is dependent on the purpose of the iron catalyst.

## Conclusions

The Fischer–Tropsch mechanism along with the role of surface carbon and vacancies have been studied on the hcp-Fe<sub>7</sub>C<sub>3</sub> (211). The major conclusion is shown below:

First, the C<sup>1</sup>–C<sup>2</sup> coupling pathway was presented as a possible C–C coupling pathway. In the C<sup>1</sup>–C<sup>2</sup> coupling pathway, it was found that the HC<sup>1</sup> + C<sup>2</sup> pathway is the preferred C<sup>1</sup>–C<sup>2</sup> coupling pathway with the effective energy barrier of 0.97 eV, which is much lower than that of the other possible C–C coupling pathway found before. Hence, the HC<sup>1</sup> + C<sup>2</sup> pathway is thought to be the major C–C coupling pathway and the HC<sup>1</sup>C<sup>2</sup> species are the major C<sub>2</sub> species from the C–C coupling pathway on the hcp-Fe<sub>7</sub>C<sub>3</sub> (211).

Second, the stepwise hydrogenation pathway was discussed. Ethylene and ethane are the two major possible C<sub>2</sub> products. Since the adsorption energy of ethylene (1.67 eV) is higher than the intrinsic energy barrier of the ethylene hydrogenation reaction (0.47 eV), the desorption process of the ethylene hardly takes place. As a result, the ethane formation pathway is the preferred stepwise hydrogenation pathway on hcp-Fe<sub>7</sub>C<sub>3</sub> (211).

Third, the surface recovery pathway was discussed to allow the Fischer–Tropsch mechanism to make sense. The direct dissociation reaction of adsorption CO on the Cv1 site and Cv2 site is thought to be the preferred carbon vacancy recovery pathway with the effective energy barriers of 1.37 eV and 1.18 eV, respectively. The dissociated oxygen from the carbon vacancy recovery pathway would be removed from the surface in the form of CO<sub>2</sub> with the effective energy barrier of 1.50 eV. Since the effective energy barrier of the surface recovery pathway is lower than that of the stepwise hydrogenation pathway of C<sub>2</sub> species, the hcp-Fe<sub>7</sub>C<sub>3</sub> (211) would likely recover from the defect-hcp-Fe<sub>7</sub>C<sub>3</sub> (211).

Fourth, the full map of the Fischer–Tropsch mechanism on the hcp-Fe<sub>7</sub>C<sub>3</sub> (211) was presented. In the achieved Fischer–Tropsch mechanism, the stepwise hydrogenation pathway is the rate-determining step for the high effective energy barrier (2.41 eV), which would also cause the increase in the carbon chain length. Moreover, due to the adsorption energy of ethylene, it could be inferred that the alkanes would be the major hydrocarbon products on the hcp-Fe<sub>7</sub>C<sub>3</sub> (211).

Fifth, the roles of the surface carbon and vacancies were concluded according to the Fischer–Tropsch mechanism. It was found that the carbon vacancy sites were the CO activation pathway sites and the surface carbon sites were the C–C coupling pathway sites. The surface carbon not only acted as the chain initiation site but also acted as the chain growth site on the hcp-Fe<sub>7</sub>C<sub>3</sub> (211). From another point of view, the circulation of the surface carbon indicated that the defect-hcp-Fe<sub>7</sub>C<sub>3</sub> (211) was the high active facet of the Fischer–Tropsch synthesis in which the carbon vacancy was the active site.

Finally, we hope that all these findings from DFT calculations could provide a detailed and comprehensive understanding of the Fischer–Tropsch mechanism on the hcp-Fe<sub>7</sub>C<sub>3</sub> phase and the role played by surface carbon in the Fischer–Tropsch synthesis. We hope that other researchers can utilize the information produced in this article to decide whether to promote, suppress, or modify the hcp-Fe<sub>7</sub>C<sub>3</sub> phase in the iron catalysts. Also, we hope that the changes in the surface structure would be taken into account when researching the Fischer–Tropsch mechanism on the iron carbide phase through the theoretical method.

## Conflicts of interest

There are no conflicts to declare.

## Acknowledgements

The authors gratefully acknowledge the College of Biological, Chemical Sciences and Engineering of Jiaying University and the R&D Center for Petrochemical Technology of Tianjin University for providing high performance computing service.

## References

- 1 M. E. Dry, *Appl. Catal., A*, 2004, **276**, 1–3.
- 2 M. Stecker, *Angew. Chem., Int. Ed.*, 2008, **47**, 9200–9211.
- 3 M. E. Dry, *Catal. Today*, 2002, **71**, 227–241.
- 4 H. Schulz, *Appl. Catal., A*, 1999, **186**, 3–12.
- 5 J. Bao, G. Yang, Y. Yoneyama and N. Tsubaki, *ACS Catal.*, 2019, **9**, 3026–3053.
- 6 H. M. T. Galvis and K. P. de Jong, *ACS Catal.*, 2013, **3**, 2130–2149.
- 7 H. M. T. Galvis, A. C. J. Koeken, J. H. Bitter, T. Davidian, M. Ruitenbeek, A. I. Dugulan and K. P. de Jong, *J. Catal.*, 2013, **303**, 22–30.
- 8 G. B. Yu, B. Sun, Y. Pei, S. H. Xie, S. R. Yan, M. H. Qiao, K. N. Fan, X. X. Zhang and B. N. Zong, *J. Am. Chem. Soc.*, 2010, **132**, 935–937.
- 9 B. Gu, V. V. Ordonsky, M. Bahri, O. Ersen, P. A. Chemayskii, D. Filimonov and A. Y. Khodakov, *Appl. Catal., B*, 2018, **234**, 153–166.
- 10 V. V. Ordonsky, Y. Luo, B. Gu, A. Carvalho, P. A. Chernavskii, K. Cheng and A. Y. Khodakov, *ACS Catal.*, 2017, **7**, 6445–6452.
- 11 Z. P. Tian, C. G. Wang, J. Yue, X. H. Zhang and L. L. Ma, *Catal. Sci. Technol.*, 2019, **9**, 2728–2741.



- 12 P. C. Psarras, J. Wilcox and D. W. Ball, *Phys. Chem. Chem. Phys.*, 2017, **19**, 5495–5503.
- 13 Y. R. He, P. Zhao, J. J. Liu, W. P. Guo, Y. Yang, Y. W. Li, C. F. Huo and X. D. Wen, *Phys. Chem. Chem. Phys.*, 2018, **20**, 25246–25255.
- 14 E. de Smit, F. M. F. de Groot, R. Blume, M. Havecker, A. Knop-Gericke and B. M. Weckhuysen, *Phys. Chem. Chem. Phys.*, 2010, **12**, 667–680.
- 15 L. Oar-Arteta, M. J. Valero-Romero, T. Wezendonk, F. Kapteijn and J. Gascon, *Catal. Sci. Technol.*, 2018, **8**, 210–220.
- 16 F. Jiang, B. Liu, W. P. Li, M. Zhang, Z. J. Li and X. H. Liu, *Catal. Sci. Technol.*, 2017, **7**, 4609–4621.
- 17 J. Mulpuri, *Ind. Eng. Chem. Res.*, 1990, **29**, 1735–1753.
- 18 T. A. Wezendonk, X. H. Sun, A. I. Dugulan, A. J. F. van Hoof, E. J. M. Hensen, F. Kapteijn and J. Gascon, *J. Catal.*, 2018, **362**, 106–117.
- 19 S. Janbroers, J. N. Louwen, H. W. Zandbergen and P. J. Kooyman, *J. Catal.*, 2009, **268**, 235–242.
- 20 O. Zhuo, L. J. Yang, F. J. Gao, B. L. Xu, Q. Wu, Y. N. Fan, Y. Zhang, Y. F. Jiang, R. S. Huang, X. Z. Wang and Z. Hu, *Chem. Sci.*, 2019, **10**, 6083–6090.
- 21 L. W. Niu, X. W. Liu, J. J. Liu, X. Liu, X. D. Wen, Y. Yang, J. Xu and Y. W. Li, *J. Catal.*, 2019, **371**, 333–345.
- 22 Y. J. Li, Z. S. Li, A. Ahsen, L. Lammich, G. J. A. Mannie, J. W. H. Niemantsverdriet and J. V. Lauritsen, *ACS Catal.*, 2019, **9**, 1264–1273.
- 23 J. Zhang, M. Abbas and J. G. Chen, *Catal. Sci. Technol.*, 2017, **7**, 3626–3636.
- 24 C. S. Kuivila, P. C. Stair and J. B. Butt, *J. Catal.*, 1989, **118**, 299–311.
- 25 C. S. Huang, L. Xu and B. H. Davis, *Fuel Sci. Technol. Int.*, 1993, **11**, 639–664.
- 26 R. Christoffersen and P. R. Buseck, *Science*, 1983, **222**, 1327–1329.
- 27 C. Yang, H. B. Zhao, Y. L. Hou and D. Ma, *J. Am. Chem. Soc.*, 2012, **134**, 15814–15821.
- 28 E. de Smit, A. M. Beale, S. Nikitenko and B. M. Weckhuysen, *J. Catal.*, 2009, **262**, 244–256.
- 29 T. Herranz, S. Rojas, F. J. Perez-Alonso, M. Ojeda, P. Terreros and J. L. G. Fierro, *J. Catal.*, 2006, **243**, 199–211.
- 30 J. D. Louw, J. P. Vandenberg, L. C. Ferreira and J. J. Pienaar, *J. Am. Chem. Soc.*, 1957, **79**, 5899–5902.
- 31 A. K. Datye, L. Mansker and Y. M. Jin, *Stud. Surf. Sci. Catal.*, 2000, **130**, 1139–1144.
- 32 B. Williams, D. Clifford, A. A. El-Gendy and E. E. Carpenter, *J. Appl. Phys.*, 2016, **120**, 6.
- 33 Q. Chang, C. H. Zhang, C. W. Liu, Y. X. Wei, A. V. Cheruvathur, A. I. Dugulan, J. W. Niemantsverdriet, X. W. Liu, Y. R. He, M. Qing, L. R. Zheng, Y. F. Yun, Y. Yang and Y. W. Li, *ACS Catal.*, 2018, **8**, 3304–3316.
- 34 T. H. Pham, X. Z. Duan, G. Qian, X. G. Zhou and D. Chen, *J. Phys. Chem. C*, 2014, **118**, 10170–10176.
- 35 T. H. Pham, Y. Y. Qi, J. Yang, X. Z. Duan, G. Qian, X. G. Zhou, D. Chen and W. K. Yuan, *ACS Catal.*, 2015, **5**, 2203–2208.
- 36 M. H. Zhang, J. Ren and Y. Z. Yu, *ACS Catal.*, 2020, **10**, 689–701.
- 37 Y. R. He, P. Zhao, J. Q. Yin, W. P. Guo, Y. Yang, Y. W. Li, C. F. Huo and X. D. Wen, *J. Phys. Chem. C*, 2018, **122**, 20907–20917.
- 38 B. X. Chen, D. Wang, X. Z. Duan, W. Liu, Y. F. Li, G. Qian, W. K. Yuan, A. Holmen, X. G. Zhou and D. Chen, *ACS Catal.*, 2018, **8**, 2709–2714.
- 39 L. J. Deng, C. F. Huo, X. W. Liu, X. H. Zhao, Y. W. Li, J. G. Wang and H. J. Jiao, *J. Phys. Chem. C*, 2010, **114**, 21585–21592.
- 40 T. Li, X. D. Wen, Y. Yang, Y. W. Li and H. J. Jiao, *ACS Catal.*, 2020, **10**, 877–890.
- 41 Y. F. Wang, Y. Li, S. Y. Huang, J. Wang, H. Y. Wang, J. Lv and X. B. Ma, *Chem. Phys. Lett.*, 2017, **682**, 115–121.
- 42 C. F. Huo, Y. W. Li, J. G. Wang and H. J. Jiao, *J. Am. Chem. Soc.*, 2009, **131**, 14713–14721.
- 43 M. Zhang, J. Ren and Y. Yu, *Mol. Catal.*, 2021, **505**, 111506.
- 44 V. V. Ordonsky, B. Legras, K. Cheng, S. Paul and A. Y. Khodakov, *Catal. Sci. Technol.*, 2015, **5**, 1433–1437.
- 45 F. H. Herbstein and J. A. Snyman, *Inorg. Chem.*, 1964, **3**, 894–896.
- 46 P. E. Blochl, *Phys. Rev. B: Condens. Matter Mater. Phys.*, 1994, **50**, 17953–17979.
- 47 G. Kresse and J. Furthmüller, *Comput. Mater. Sci.*, 1996, **6**, 15–50.
- 48 F. Kresse, *Phys. Rev. B: Condens. Matter Mater. Phys.*, 1996, **54**, 11169–11186.
- 49 J. P. Perdew, K. Burke and M. Ernzerhof, *Phys. Rev. Lett.*, 1996, **77**, 3865–3868.
- 50 P. Methfessel, *Phys. Rev. B: Condens. Matter Mater. Phys.*, 1989, **40**, 3616–3621.
- 51 H. J. Monkhorst and J. D. Pack, *Phys. Rev. B: Condens. Matter Mater. Phys.*, 1976, **13**, 5188–5192.
- 52 S. Grimme, J. Antony, S. Ehrlich and H. Krieg, *J. Chem. Phys.*, 2010, **132**, 19.
- 53 S. Grimme, S. Ehrlich and L. Goerigk, *J. Comput. Chem.*, 2011, **32**, 1456–1465.
- 54 D. Sheppard, R. Terrell and G. Henkelman, *J. Chem. Phys.*, 2008, **128**, 10.
- 55 D. Sheppard, P. H. Xiao, W. Chemelewski, D. D. Johnson and G. Henkelman, *J. Chem. Phys.*, 2012, **136**, 8.
- 56 J. Cheng, P. Hu, P. Ellis, S. French, G. Kelly and C. M. Lok, *J. Phys. Chem. C*, 2010, **114**, 1085–1093.
- 57 J. Cheng, P. Hu, P. Ellis, S. French, G. Kelly and C. M. Lok, *J. Phys. Chem. C*, 2009, **113**, 8858–8863.
- 58 J. Cheng, X. Q. Gong, P. Hu, C. M. Lok, P. Ellis and S. French, *J. Catal.*, 2008, **254**, 285–295.

